Seismological Research Letters

Real time imaging, forecasting and management of human-induced seismicity at Preston New Road, Lancashire, England

--Manuscript Draft--

Manuscript Number:	
Full Title:	Real time imaging, forecasting and management of human-induced seismicity at Preston New Road, Lancashire, England
Article Type:	Article - Regular Section
Corresponding Author:	James Philip Verdon, Ph.D. University of Bristol Bristol, UNITED KINGDOM
Corresponding Author Secondary Information:	
Corresponding Author's Institution:	University of Bristol
Corresponding Author's Secondary Institution:	
First Author:	Huw Clarke
First Author Secondary Information:	
Order of Authors:	Huw Clarke
	James Philip Verdon, Ph.D.
	Tom Kettlety
	Alan F. Baird
	Michael Kendall
Order of Authors Secondary Information:	
Manuscript Region of Origin:	UNITED KINGDOM
Suggested Reviewers:	Mirko van der Baan University of Alberta Mirko.VanderBaan@ualberta.ca
	Grzegorz Kwiatek GFZ Potsdam grzegorz.kwiatek@gfz-potsdam.de
	Katie Keranen Cornell kmk299@cornell.edu
Opposed Reviewers:	

Dear Editors,

Please consider the enclosed manuscript, entitled "Real time imaging, forecasting and management of human-induced seismicity at Preston New Road, Lancashire, England", on behalf of myself and my co-authors for publication in Seismological Research Letters. This manuscript presents results from original research and is not under consideration for publication elsewhere.

The issue of induced seismicity is a significant one for a range of industries. There is currently significant debate as to the most appropriate ways to mitigate seismic hazard associated with subsurface industries.

In this paper we use microseismic observations to populate a statistical model, and extrapolate the model to forecast the largest expected event size during a hydraulic fracturing operation. We performed this forecasting in real time during operations, reporting our forecasts to the relevant regulator as operations progressed.

The event magnitudes that occurred fell within the maximum event size envelope forecasted by our models. To our knowledge, this represents the first successful forecast of induced event magnitudes made in real time during a subsurface injection operation of any kind. As such, it represents a significant advance in terms of our scientific understanding of induced seismicity, which may also be of immense practical significance in terms of future best practice to mitigate induced seismicity.

We also note that this paper is the first to describe what is an operational site of high prominence: activities at the site continue to be reported across the UK national media, as well as in major international publications, and being the subject of debates in the UK's national parliament. As such, we anticipate a high level of interest in this paper simply because of the prominence of the site it describes.

Dataset: The full dataset is scheduled for release by the Oil and Gas Authority on 27th June 2019. Our hope, assuming that the review process proceeds in a timely manner, is that this paper be released at the same time as this high-interest dataset becomes public.

Reviewers: we suggest Mirko van der Baan (University of Alberta), Gregorz Kwiatek (GFZ, Potsdam), and Katie Keranen (Cornell University).

Conflict of Interest: We note that Huw Clarke is an employee of the operating company that performed the hydraulic stimulation.

Yours Faithfully,

Dr. James Verdon

School of Earth Sciences, University of Bristol

Real time imaging, forecasting and management of human-induced seismicity at Preston New Road, Lancashire, England

Authors: Huw Clarke[1], James P. Verdon[2], Tom Kettley[2], Alan F. Baird[2], J-Michael Kendall[2]

1. Cuadrilla Resources Ltd., Cuadrilla House, 6 Sceptre Court, Bamber Bridge, Lancashire, U.K., PR5 6AW.

2. School of Earth Sciences, University of Bristol, Wills Memorial Building, Queen's Road, Bristol, U.K., BS8 1RJ.

ABSTRACT

Earthquakes induced by subsurface fluid injection pose a significant issue across a range of industries. Debate continues as to the most effective methods to mitigate the seismic hazard associated with fluid injection. This study describes the first scientifically-studied example where microseismic observations were used to make successful forecasts of expected event magnitudes during injection. These forecasts were used to guide operational decision-making in real time, ensuring that levels of seismicity remained within acceptable levels. To date, induced seismicity has typically been regulated using retroactive Traffic Light Schemes. This study shows that the use of high quality microseismic observations, providing event populations spanning several orders of magnitude, can provide a more effective approach.

1. Introduction

Human-induced seismicity is becoming an increasingly controversial topic. It is well known that activities such as mining and water impoundment can lead to felt seismicity, but increasingly activities such as geothermal energy (Grigoli *et al*., 2018), underground storage of waste such as CO_2 or water (Keranen *et al*., 2014) and hydraulic stimulation of shale gas reservoirs (Bao and Eaton, 2016), are attracting concern from the public, regulators and operators.

The stimulation of fractures by injecting water at high-pressure is a technique used to create conductive fracture networks in low-permeability reservoir rocks. Hydraulic fracture stimulation is widely used in the commercial production of hydrocarbons, and also to develop engineered geothermal systems. Use of this method has become more prominent in the past decade, associated primarily with the shale gas boom (Wang and Krupnick, 2013) in North America.

If hydraulic fractures intersect a pre-existing fault that is near to its critical stress state, the increase in pore pressure can reduce the effective normal stress, declamping the fault and creating induced seismicity. Such cases are relatively rare: Atkinson *et al*. (2016) estimate that only 0.3% of wells in British Columbia and Alberta, a region with some of the highest levels of hydraulic fracturing-induced seismicity (HF-IS), are associated with induced events larger than magnitude 3. Nonetheless, the issue of induced seismicity is a concern for the petroleum and geothermal industries, and will likely be of concern to other nascent industries, such as carbon capture and storage (Verdon, 2014), as well.

Debate continues with regards to the most effective method(s) to mitigate HF-IS, and what regulations should be applied. To date, regulators have typically imposed Traffic Light Schemes (TLSs) whereby the operator reduces, pauses or stops injection if the magnitude of the largest event exceeds a specified threshold. TLS thresholds have varied significantly in different jurisdictions (Baisch *et al*., 2019): for example, in Alberta the red light is set at M = 4, whereas in the United Kingdom (U.K.) the red light is set at M = 0.5, a difference in earthquake moment of over 175,000 times.

TLSs are essentially retroactive in nature, because the operator takes actions after an event has occurred. In some case studies, seismicity has been observed to continue, and increase in magnitude, after injection has ceased (e.g., Häring *et al*., 2008; Clarke *et al*., 2014). These post-injection increased-magnitude events, known as “trailing events”, pose an issue for TLSs because they compel the regulator to set thresholds that may be substantially lower than the

actual magnitude they wish to avoid. Hence operations may be stopped even though levels of seismicity are well below that which might be considered hazardous.

It is therefore desirable to manage and mitigate induced seismicity in real time, as operations proceed. For example, injection volumes could be reduced or stimulation can be directed away from areas showing fault reactivation. Here we show a successful example of managing HF-IS with a recently acquired dataset from a shale gas operation in the UK.

1.1 Using microseismic data for decision-making to mitigate induced seismicity

TLS decisions are based solely on the magnitude of the largest events. This is a rational option if monitoring is provided by national or regional seismometer networks, where monitoring stations may be 10s of km from the site (e.g., Clarke *et al*., 2014; Friberg *et al*., 2014; Skoumal *et al*., 2015; Schultz *et al*., 2015). In such cases only the larger events may be detected, and hypocentral locations and focal mechanisms may be poorly constrained. Hence the only reliable, well-constrained data are the magnitudes of the larger events.

However, it is not uncommon for operators to deploy microseismic monitoring, where downhole geophone arrays (Maxwell *et al*., 2010) or dense surface arrays (Chambers *et al*., 2010) are able to detect very low magnitude "microseismic" events. High-quality microseismic monitoring may record thousands or even hundreds of thousands of events with very precise locations, spanning several orders of magnitude, provided in real time during operations (e.g., Zinno et al., 1998). These data will be highly relevant for understanding the risks posed by HF-IS. However, such data is not utilized by TLSs in their current design.

There are two primary ways by which microseismic observations can be used to guide decisions to mitigate induced seismicity. Firstly, microseismic data can be used to detect and characterise the interactions between hydraulic fractures and pre-existing faults (Maxwell *et al*., 2008; Maxwell *et al*., 2009, Wessels *et al*., 2011; Kettlety *et al*., 2019; Igonin *et al*., 2019). Microseismic events during hydraulic fracturing typically occur in clusters extending from the well perpendicular to the minimum horizontal stress, tracking the growth of the hydraulic fractures and mapping the extent of the stimulated reservoir volume. If a fault is intersected events may begin to line up along the structure, allowing it to be identified and mapped (Maxwell *et al*., 2008; Wessels *et al*., 2011; Hammack *et al*., 2014; Kettlety *et al*., 2019). In many cases fault reactivation can also be identified by a decrease in Gutenberg and Richter (1944) *b* values (Maxwell *et al*., 2009; Verdon and Budge, 2018; Kettlety *et al*.,

2019), or by an increase in the rate of microseismicity relative to the injection rate (Maxwell *et al*., 2008; Verdon and Budge, 2018).

If a fault is identified during injection, then an operator can re-design their injection program such that the fault will be avoided. This can be achieved by, for example, skipping stages along a horizontal well, changing the planned injection rates or volumes, or by altering the properties of the injected fluid (for example a more viscous fluid will carry more proppant while travelling less distance into the formation).

Microseismic data can also be used to make forecasts of the expected event magnitudes during stimulation. Induced seismicity has been observed to follow the Gutenberg and Richter (G-R hereafter) distribution (van der Elst *et al*., 2016), with both the number of events (Shapiro *et al*., 2010) and the cumulative seismic moment released (Hallo *et al*., 2014) being proportional to the cumulative injection volume. As such, the largest expected event magnitude can be forecast by characterising these relationships for the site in question, and then extrapolating them to the planned injection volume. This approach has shown significant promise when applied in a pseudo-prospective manner (Verdon and Budge, 2018).

1.2 A case study from northwest England

In this paper we report on the Preston New Road PNR-1z well, Lancashire, U.K., operated by Cuadrilla Resources Ltd (CRL hereafter). This was the first U.K. onshore well to be hydraulically fractured since a government review of HF-IS seismicity was concluded in 2012. As such it is the subject of regular national media attention (e.g., Webster, 2018) and debate in the national parliament (Hansard, 2018). Given the high levels of public scrutiny, the site was extensively monitored both by CRL, and by independently-funded organisations such as the British Geological Survey (BGS). This monitoring included groundwater, surface water, air quality, and traffic movements, as well as the induced seismicity monitoring outlined below. Extensive baseline surveys were conducted for all of the above, so that any change from the pre-operational conditions could be identified.

Given public concerns about HF-IS in the U.K., CRL took proactive measures to mitigate induced seismicity, guided by microseismic observations as outlined above. We begin with a brief description of the operations conducted at the site, then show how microseismic data were used to identify and map the interaction between hydraulic fractures and a fault, and to forecast expected event magnitudes as the injection progressed. This information allowed CRL to adjust their injection program, ensuring that levels of seismicity did not exceed the

overall objectives set by the regulator, as well as providing an increased understanding of more proactive measures that could be applied in future as an alternative to a very stringent TLS.

2. Description of the Preston New Road Site

The Preston New Road PNR-1z well targets the Carboniferous Lower Bowland Shale at a depth of approximately 2,300 m. The lateral portion of the well extends 780 m in a westward direction (Figure 1). A sliding-sleeve completion was used, with 41 individual sections spaced at 17.5 m intervals. CRL planned to stimulate each of these sleeves with 400 m^3 of slickwater, placing 50 tonnes of proppant per sleeve. Stimulation was carried out in two periods from 15th October to 2nd November, and then from 8th to 17th December 2018. Figure 2 shows an overview of injection stages conducted in the PNR-1z well.

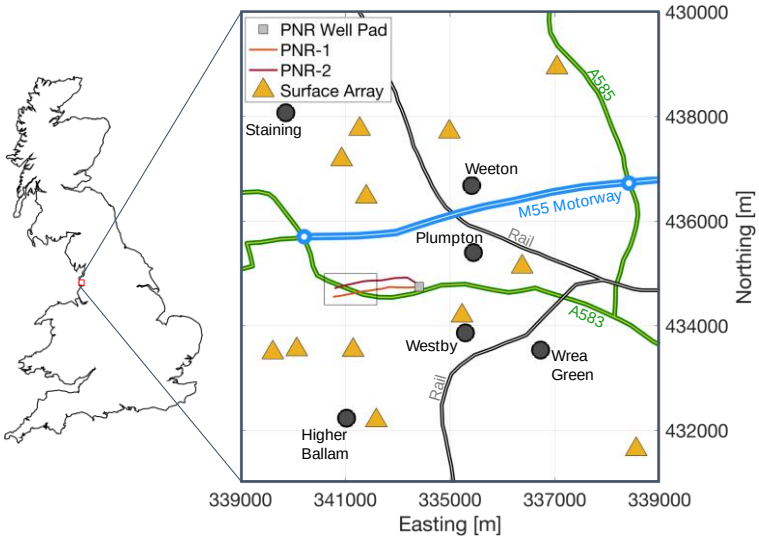

Figure 1: Map of operations at Preston New Road showing the positions of the drilling pad and horizontal tracks of PNR-1z and PNR-2, and the positions of the surface monitoring stations. The black box marks the area of interest shown in subsequent figures. Major roads, rail links, and nearby villages are also marked. Coordinates are U.K. Grid Reference.

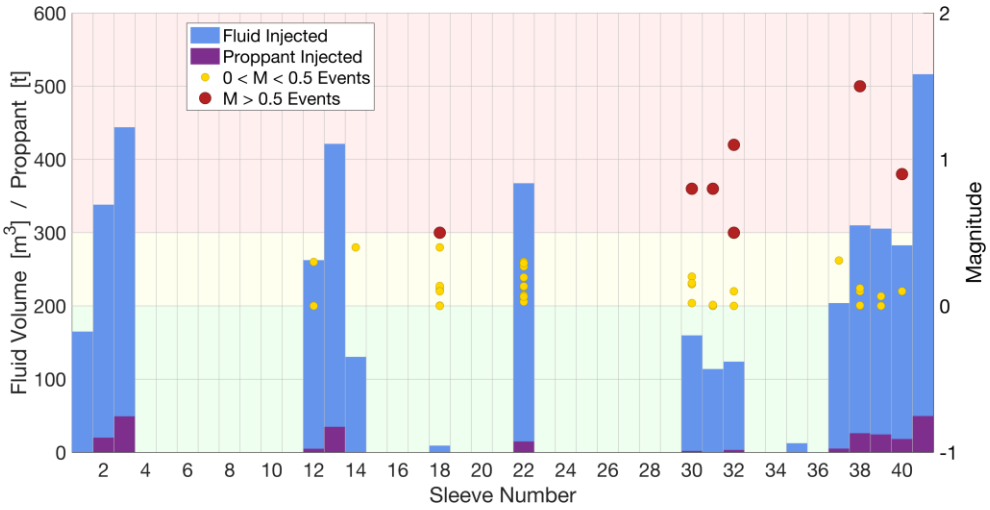

(a)

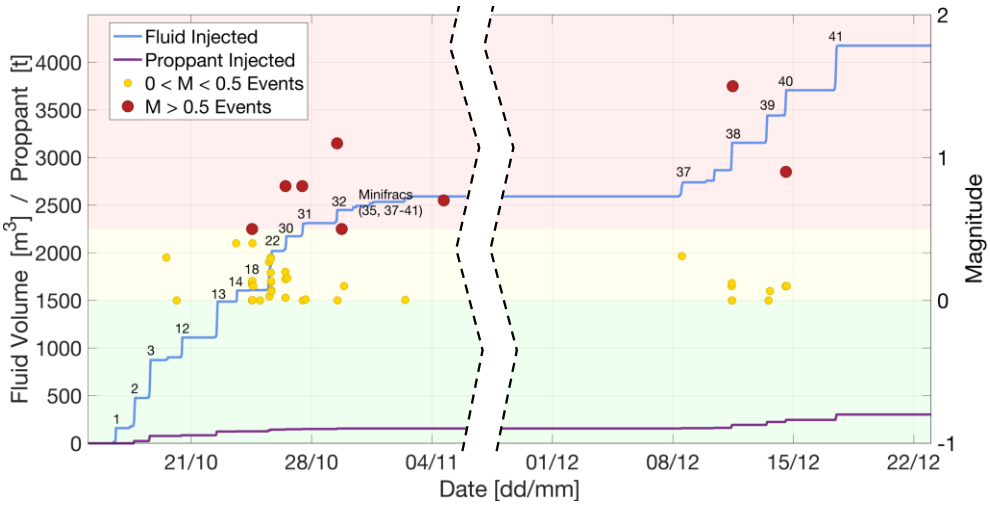

(b)

Figure 2: Overview of injection into PNR-1z. (a) shows the volume of fluid (blue) and mass of proppant (purple) injected into each sleeve. It also shows TLS events (yellow and red dots) that occurred during or after injection into each sleeve. (b) shows cumulative fluid volume (blue) and proppant mass (purple) injected as a function of time, again showing the occurrence of TLS events. The numbering in (b) shows the sleeve being injected. The background colours show the TLS green, amber and red magnitude thresholds.

2.1 U.K. Regulations for Induced Seismicity

In the U.K., HF-IS is regulated by the Oil and Gas Authority (OGA). The OGA's objective is to minimize the number of events felt at the surface by the public, and to avoid the possibility of events capable of causing damage to nearby buildings or infrastructure (Oil and Gas

Authority, 2018). U.K. standards for ground vibrations from other activities such as quarry blasting, construction equipment and industrial machinery are provided by British Standard BS 7385-2. This sets a peak ground velocity (PGV) threshold, above which may cause cosmetic damage such as cracking of plaster, of 15 mm/s (at lower frequencies such as would be expected from induced seismicity). Using ground motion prediction equations (e.g., Akkar *et al.*, 2014), for hypocentral depths equivalent to expected depths of hydraulic fracturing and making conservative assumptions for ground conditions, this threshold is approximately equivalent to a magnitude of $M = 3.5$. Therefore, this objective could be reasonably translated as minimizing the number of events that have magnitudes $2 < M < 3$, and avoiding events that have magnitudes $M > 3.5$.

To regulate HF-IS the OGA currently applies a TLS with a red-light threshold of $M = 0.5$. This is by some margin the most stringent level for ground motion applied to any industrial activity that we are aware of. The $M = 0.5$ red-light threshold is 175 times smaller than the $M = 2$ events that the scheme seeks to minimize, and over 30,000 times smaller than the $M > 3.5$ events that the scheme seeks to avoid. This disparity exists to mitigate the risk posed by trailing events, where event magnitudes may continue to increase after injection has been stopped (Green *et al.*, 2012). This TLS was applied to stimulation of the PNR-1z well, and the restrictive nature of this scheme had a significant impact on the operations: only 17 of the planned 41 stages were injected, and of these only 2 injected the planned total 50 tonnes of proppant.

2.2 Real time seismic and microseismic monitoring

Two systems were used in combination to monitor induced seismicity at Preston New Road. Both of these systems provided event locations and magnitudes in real time (typically within 1-4 minutes of event occurrence) computed by a processing contractor (Schlumberger). To administer the TLS an array of 8 sensors including 2 broadband seismometers and 6 geophones (4.5 Hz instruments) was deployed at the surface, augmented by 4 broadband seismometers deployed by the British Geological Survey (Figure 1). During real time monitoring the surface array reported 54 events with a minimum magnitude of $M_L = -0.8$. The surface array provided sufficient coverage such that focal mechanisms could be determined for 9 of the largest events during real time monitoring.

Microseismicity was recorded using an array of 24 geophones (15 Hz instruments) placed in the build section (where the well deviates from vertical to horizontal) of the adjacent PNR-2

well, 200 m shallower and 220 m northeast of the nearest sleeve in PNR-1z (Figure 3). This array reported 39,164 events in real time, with a minimum magnitude of M_W = -3.0.

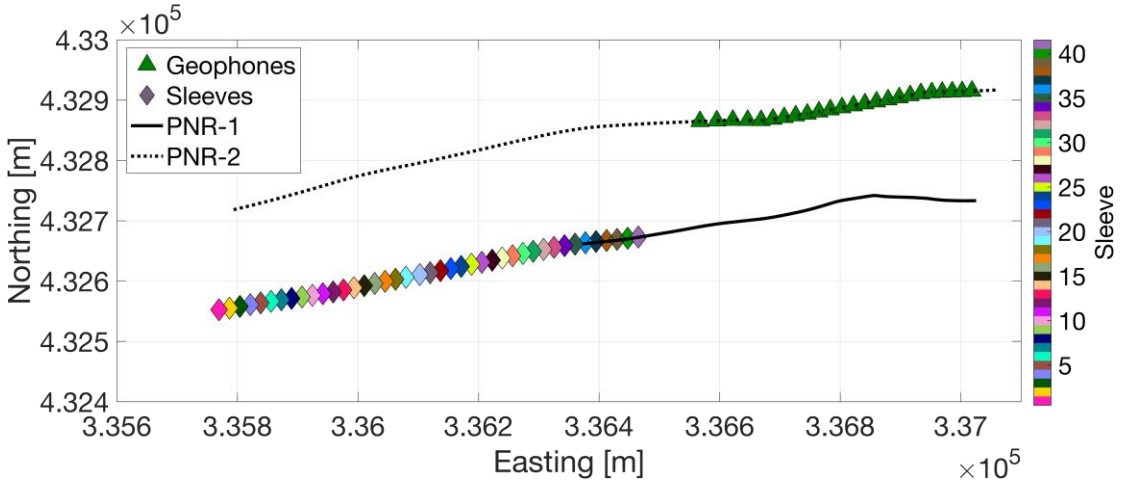

(a)

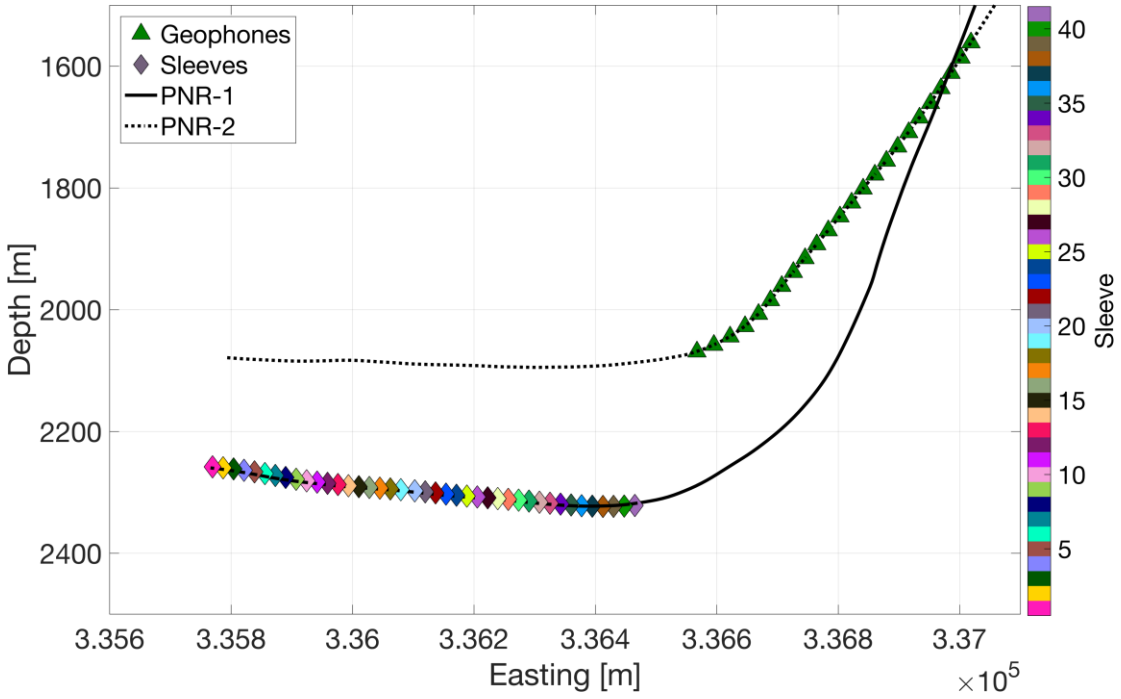

(b)

Figure 3: Map (a) and cross-section (b) of the downhole monitoring array deployed in well PNR-2, and the sleeves through which injection was conducted in PNR-1.

2.3 A note on magnitudes

Measurements of magnitudes for small events can be challenging (Kendall *et al.*, 2019). Two different magnitude scales were in use during real time operations at Preston New Road. The U.K. TLS regulations mandate the use of a local magnitude scale with a correction applied to account for the small source-receiver distances (Butcher *et al.*, 2017; Luckett *et al.*, 2019). Therefore, magnitudes from the surface array were reported as M_L values. However, these M_L scales are calibrated using surface stations, implicitly including free-surface effects and near-surface attenuation, so this M_L scale is not calibrated for downhole instruments. Instead the downhole events were reported as M_W values. While a direct comparison and conversion between the two scales might seem like an obvious solution, in practice this was more challenging. The surface array recorded the largest 54 events, so only these events had reported M_L values. However, many of these larger events produced subsurface motions that were beyond the dynamic range of the downhole instruments, and so accurate downhole M_W values could not be determined for these events. Hence, there is only a small subset of events which are large enough such that a robust M_W value can be computed using the surface array, but no too large such that a robust M_W value can also be computed using the downhole stations, thereby enabling a comparison to be made.

Work is ongoing to resolve the observed M_L and M_W values. However, the need for rapid decision-making meant that this information was not used during real time operations. Instead, we used M_L values for the 54 events that were reported by the surface array, and M_W values for the remaining events. Clearly this is a solution that was far from optimal. However, we note that doing so does not produce anomalies or unusual behaviour if the overall magnitude-frequency distribution is examined (Figure 4), suggesting that this approach was reasonable in this case. However, in future cases this issue should be addressed by ensuring that moment magnitudes are reported by both array types, and that relationships to convert between downhole M_W values and surface M_L values are calibrated.

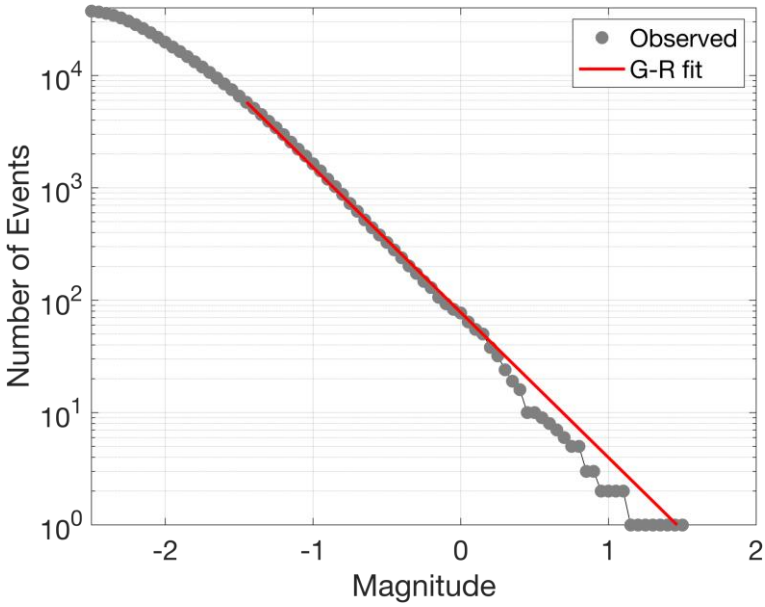

Figure 4: Magnitude-frequency distribution for all events reported in real time (grey dots). The observed distribution follows the G-R distribution with a = 1.89 and b = 1.29 (red line).

3. Microseismic observations

Figure 5 shows a map and cross-section for located events with a signal-to-noise ratio greater than 5. Events during each stage are mostly found in the vicinity of the corresponding injection sleeve, extending approximately 200 m to the north. The events extend approximately 150 m above and below the well, remaining within the Bowland Shale Formation. The largest observed event has a magnitude of M = 1.5, and in total 8 events exceeded the TLS M = 0.5 threshold, 3 of these occurred during injection and required pumping to be stopped, while the remaining 5 were trailing events that occurred after injection had stopped.

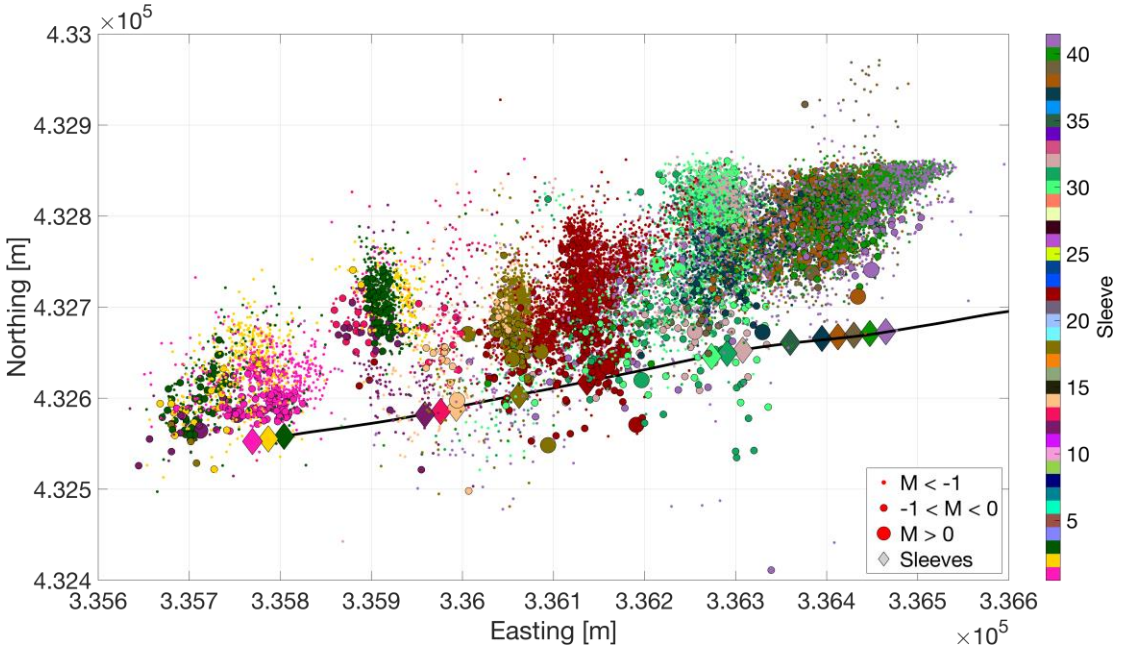

(a)

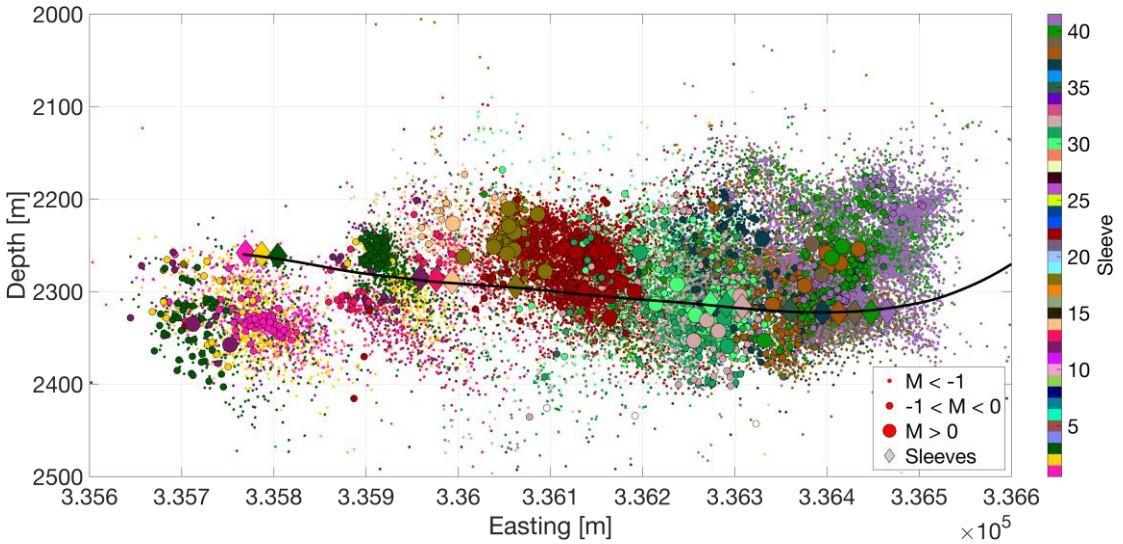

(b)

Figure 5: Microseismic event locations. Map view (a) and cross-section (b) of microseismic events detected during real time monitoring at PNR-1z. Events are coloured by the sleeve number with which they are associated. The PNR-1z well profile is shown by the black line.

3.1. Relationship between microseismicity and previously-observed faults

Prior to the start of operations, a 3D reflection seismic survey was acquired at the site. Several pre-existing faults and "seismic discontinuities" (potential small faults that are at the limit of

resolution for 3D seismic surveys) were identified (Cuadrilla Resources Ltd., 2018). We observed little or no correlation between the positions of these features and microseismic event locations. The events associated with Stages 1 – 3 at the toe of the well overlap with one of the seismic discontinuities. However, the levels of microseismicity produced by these stages were among the lowest. In contrast, none of the events that exceeded the $M > 0.5$ TLS threshold occurred on structures identified from the 3D survey.

Indeed, no microseismicity coincided with any of the large faults identified in the 3D seismic survey, all of which were significantly further from the well than the greatest distances reached by the microseismicity. This observation allowed CRL to proceed with confidence that the hydraulic stimulation was unlikely to cause re-activation of the larger tectonic faults that had been identified.

3.2. Identification of potential seismogenic structures

The northwards propagation of microseismicity from each injection sleeve traces the propagation of hydraulic fractures perpendicular to the minimum horizontal stress azimuth of 83°. However, our interest was to identify pre-existing structures on which the larger events may occur. We note that the largest event, with a magnitude of $M = 1.5$, could correspond to a rupture with displacement of less than 1 cm with a length less than 100 m. At this scale the distinction between a "small fault" and a "large fracture" is somewhat arbitrary: we will use "fault" hereafter to describe such features, while keeping this fact in mind.

In Figure 5 the events do not display an obvious alignment along a pre-existing fault, an observation which often provides the clearest evidence of fault reactivation (e.g., Igonin *et al*., 2019). Instead, we use a combination of observations to identify and define the seismogenic structures responsible for the largest events.

3.3. Focal mechanisms

The focal mechanisms for 6 of the largest events are shown in Figure 6a. The events all have similar mechanisms: either left-lateral strike slip on a near-vertical fault striking NE-SW, or right-lateral strike-slip on a near-vertical fault striking NW-SE. The consistent orientation of these focal mechanisms provides a constraint for the orientation of any potential seismogenic structure.

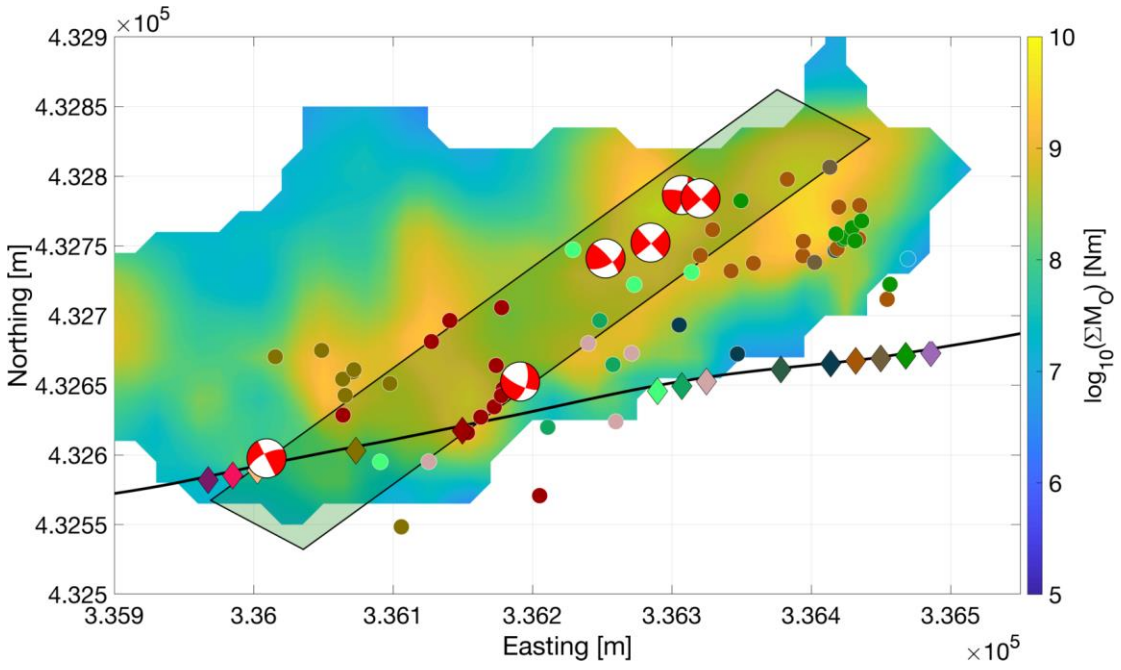

287

288 *(a)*

289

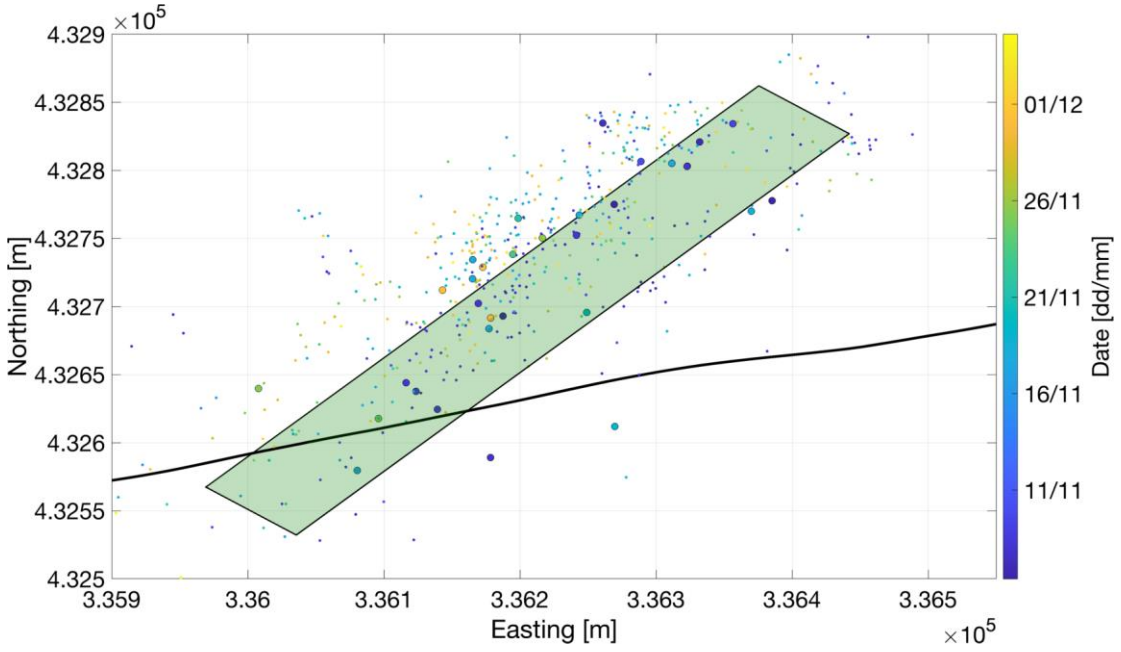

290

291 *(b)*

292 *Figure 6: Identifying a pre-existing fault. Maps showing the observations used to identify*
293 *seismogenic structures. (a) shows all events with M > 0 (dots coloured by sleeve number as*
294 *per Figure 5), the cumulative seismic moment (contours), and the focal mechanisms of the*
295 *largest events. (b) shows a map of the events that occurred during the injection hiatus from*
296 *3rd November to 7th December. We combine the largest events and the flowback events to map*
297 *a plane striking at 237° and dipping at 70° (black-outlined box).*

3.4. Mapping large events and cumulative moment release

Figure 6a also shows the positions of all events with $M > 0$, and maps the cumulative seismic moment release, ΣM_O. These observations allow us to identify a single zone in which almost all of the larger events were occurring, and within which the overall cumulative seismic moment release was highest. This zone intersects the PNR-1z well at roughly the position of Sleeve 18, which was the first stage on which an event exceeding the $M > 0.5$ TLS threshold occurred. Interaction between injection activities and this zone occurred along the well towards the heel. Importantly, the orientation of this zone matches the orientation of the NE-SW plane of the observed focal mechanisms.

3.5. Microseismicity during injection hiatus

These observations allowed us to identify the seismogenic feature during the initial stimulation of Stages 18 – 41 in October 2018 (Table 1). From the 3rd of November, CRL paused the injection program in response to repeated $M > 0.5$ events that had occurred during the previous week. The injection pause continued until 7th December. Observations of microseismicity during this injection hiatus (Figure 6b) provided the final and definitive identification of the seismogenic structure. The events during hiatus, almost all of which had magnitudes less than $M < -1$, were all located along the same feature that we had identified from the focal mechanism orientations, the positions of the largest events, and the cumulative moment release map.

Our overall interpretation of the observed microseismicity is that a pre-existing fault plane runs northeast from the well. During hydraulic stimulation, larger events occurred when the hydraulic fractures from each stage intersected this fault. During the hiatus, whereas the microseismic events associated with hydraulic fracturing stopped, low levels of microseismicity continued to persist along this feature for a longer period of time. We fit a plane to a combined population of the $M > 0$ events (Figure 6a) and the hiatus events (Figure 6b), finding a strike of 237° and a dip of 70°, which is consistent with the observed focal mechanisms. We term this fault NEF-1 (Northeast Fault-1) hereafter. With the maximum and minimum horizontal stresses oriented north-south and east-west respectively, this plane is well-oriented for the observed left-lateral strike slip motion.

4. Statistical Forecasting of Event Magnitudes

During stimulation we applied in real time an event magnitude forecasting model to guide operational decisions with respect to induced seismicity. Hallo *et al*. (2014) introduced the concept of seismic efficiency, S_{EFF}, which describes the correlation between the cumulative moment release, ΣM_O, and the cumulative injection volume ΔV:

$$S_{EFF} = \frac{\Sigma M_O}{\mu \Delta V}, \quad (1)$$

where μ is the shear modulus, assumed to be 20 GPa here. Based on the observed values of S_{EFF} and the *b* value, the size of the largest expected event, M_{MAX} can be estimated as:

$$M_{MAX} = \frac{2}{3}\left(\log_{10}\left(\frac{S_{EFF}\mu\Delta V\left[\frac{3}{2}-b\right]}{b10^{9.1}}\right)\right) + \frac{2}{3}\log_{10}\left(10^{b\delta} - 10^{-b\delta}\right), \quad (2)$$

where δ is the probabilistic half-bin size defined around M_{MAX} (Hallo *et al*., 2014). This formulation assumes that *b* and S_{EFF} do not change significantly for a given stage, or for a given volume of rock being stimulated. Verdon and Budge (2018) applied this approach in a pseudo-prospective manner to a hydraulic fracturing dataset from the Horn River Shale, Canada, showing that it would have accurately forecast event magnitudes had it been applied in real time.

Equation 2 posits a logarithmic dependence between injection volume and the largest event size. Given that the planned injection volumes do not vary by orders of magnitude between stages, the primary controlling factor on the largest event magnitude is therefore S_{EFF}. The relationship between S_{EFF}, ΔV, and M_{MAX} is plotted in Figure 7 (assuming *b* = 1).

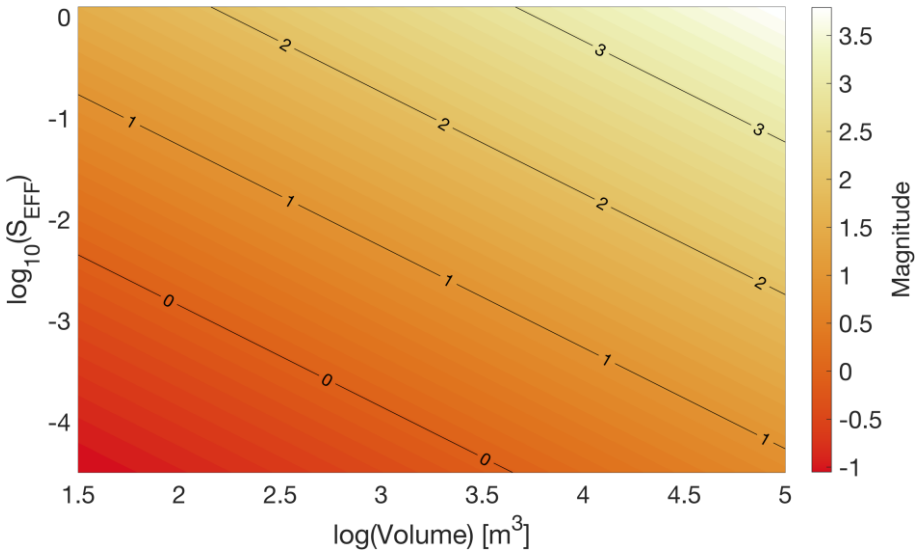

Figure 7: Volume, efficiency and maximum magnitude. Relationship between S_{EFF}, ΔV, and M_{MAX} given by Equation 2 (assuming b = 1), showing the logarithmic dependence of M_{MAX} on ΔV.

Equation (2) provides the most likely maximum event magnitude. In practice it is more useful to define a value for M_{MAX} that is unlikely to be exceeded. Using synthetic event distributions, Verdon and Budge (2018) showed that adding a value of 0.5 to Equation 2 is sufficient to capture 95% of the variance between true and re-constructed model populations. In our analysis we applied this correction such that our results provided a value that, within reasonable levels of certainty, will not be exceeded.

We tracked *b* and S_{EFF} in real time during every stage, providing regularly-updated forecasts of M_{MAX}. We compute the *b* value using the Aki (1965) maximum likelihood approach, computing the minimum completeness threshold using a Kolmogorov-Smirnov test to assess the quality of fit between the observed magnitude distribution and the G-R relationship (Clauset *et al*., 2009), requiring a minimum of 50 events for a reliable measurement (though with over 39,124 events in 17 stages, the number of events passed this threshold very quickly for each stage).

Figure 8 shows a selection of results for this analysis when performed on a stage-by-stage basis, i.e., considering ΣM_O and ΔV associated with each individual stage. We find that for most of the stages this approach provided accurate bounds, with the observed events falling within the modelled value of M_{MAX}. However, this is not always the case, as can be seen for Stages 32 and 38 in Figures 8b and 8c, for example.

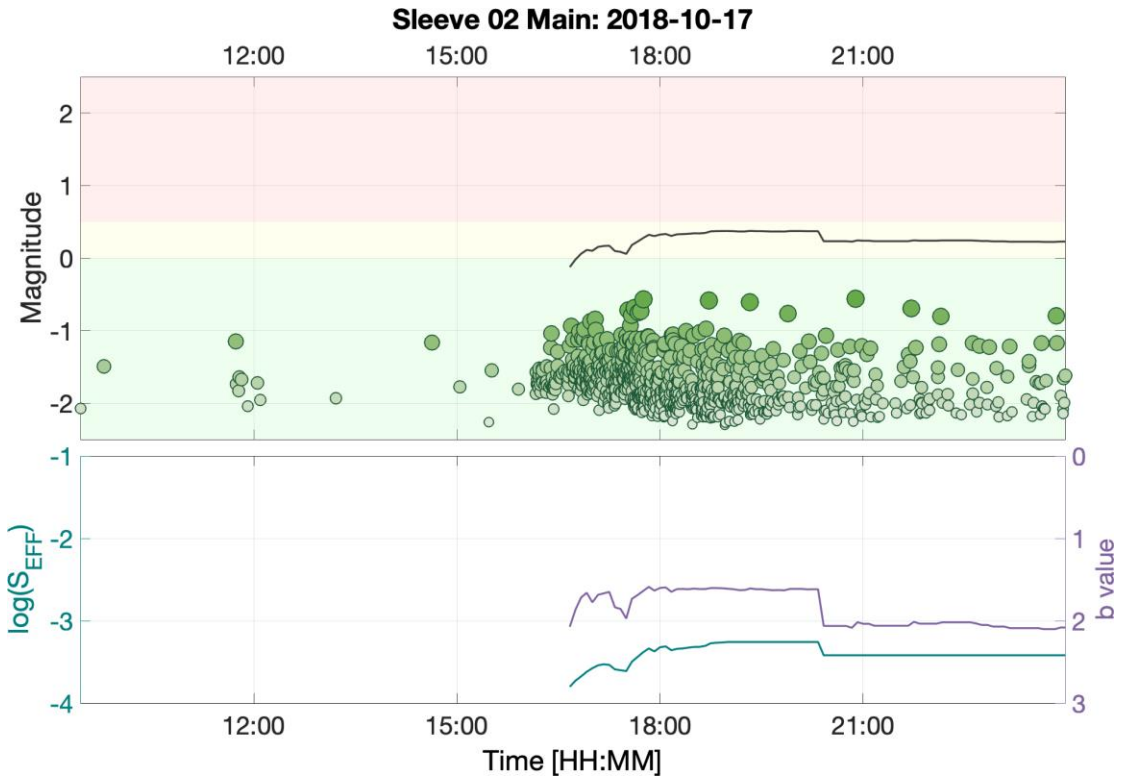

374

375 *(a)*

376

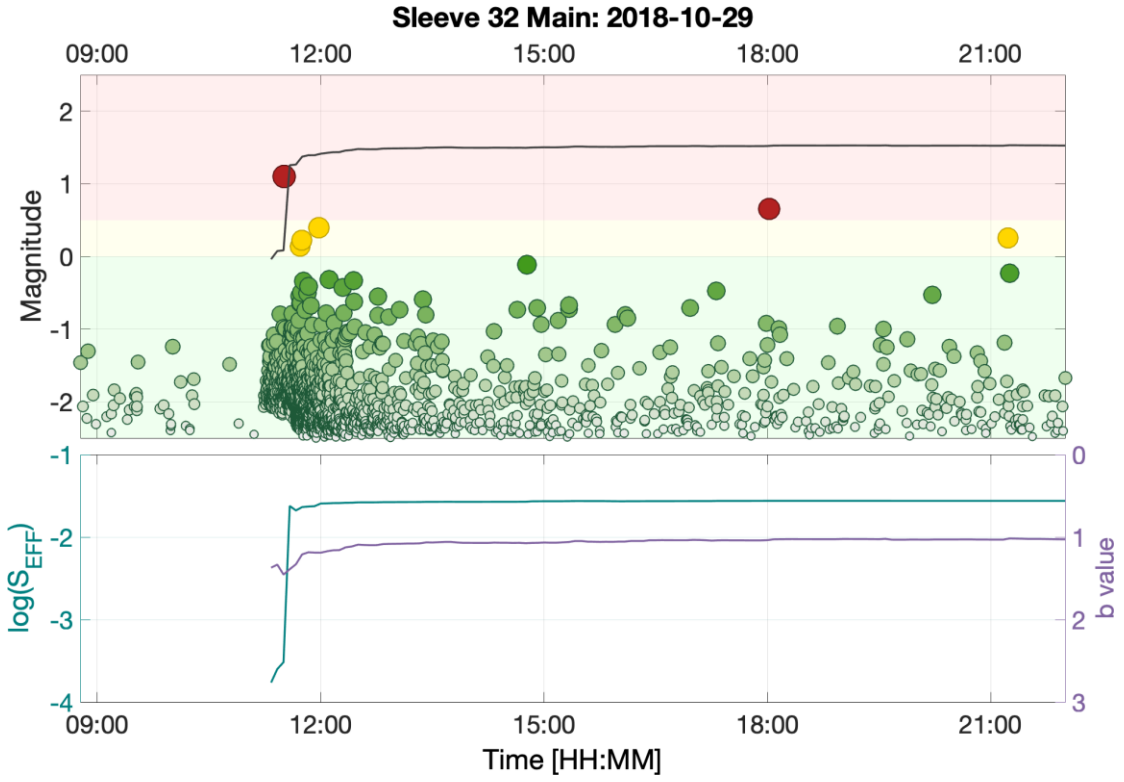

377

378 *(b)*

379

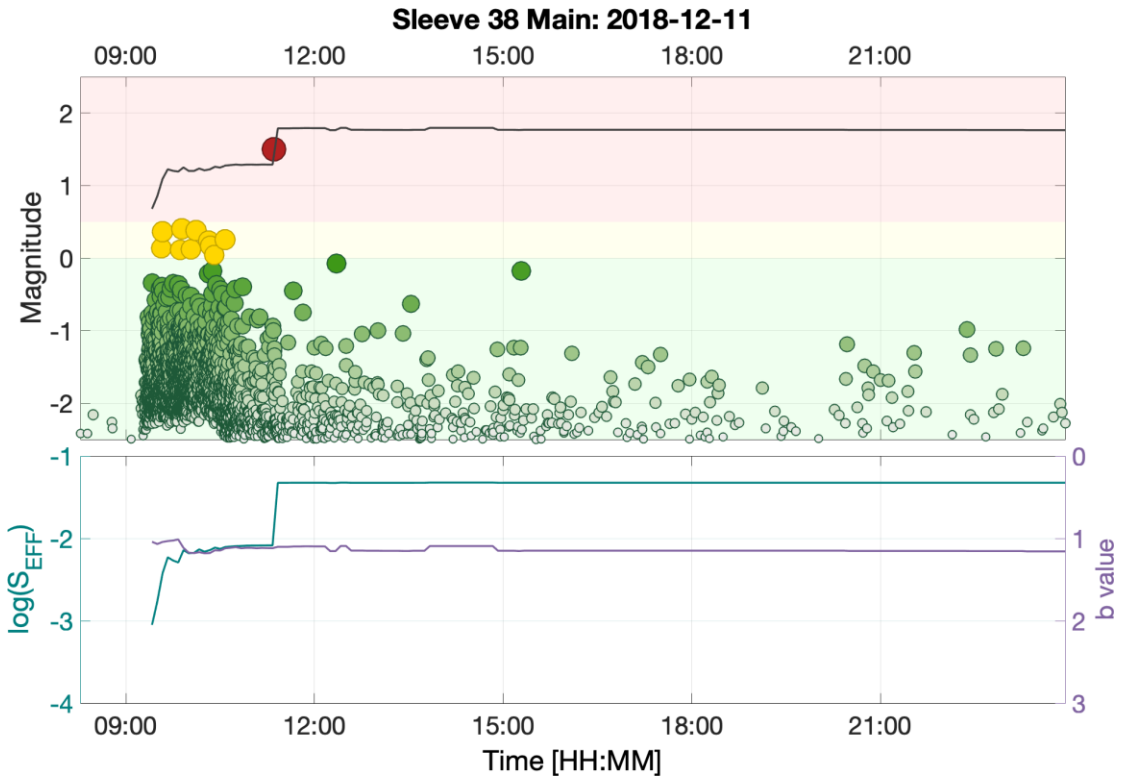

380

381 *(c)*

382

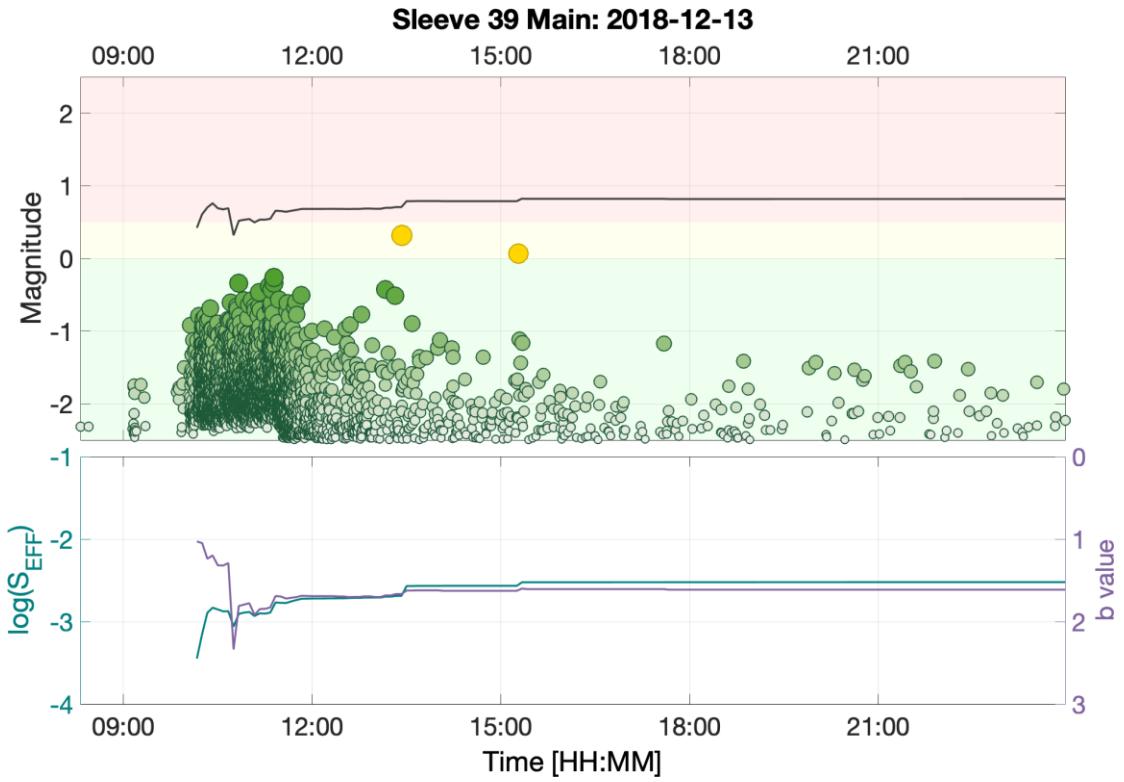

383

384 *(d)*

385

Figure 8: Forecasting M_{MAX} during stages. Examples of S_{EFF}, b, and M_{MAX} tracked during injection on a stage-by-stage basis. In the lower panels we track S_{EFF} (blue) and b (purple), and in the upper panels we plot the resulting values of M_{MAX} (black line) compared against observed events (circles coloured by magnitude relative to the TLS thresholds). In some cases, for example Stages 2 (a) and 39 (d), the forecast M_{MAX} provides the upper bound of the observed seismicity. In other cases, for example Sleeves 32 (b) and 38 (c), the largest events exceeded the M_{MAX} values modelled earlier in the injection period.

The reason for this discrepancy is obvious when considered in the light of the observations and interpretations of the microseismicity presented in Section 3: the NEF-1 fault runs obliquely to the well and was intersected by multiple stages. It is therefore not appropriate to consider each stage independently because the seismicity was caused by repeated injection into the same feature. Instead, as the NEF-1 feature was identified, we adjusted our approach to include the effects of repeated injection, treating all injection and seismicity from Stage 18 onwards cumulatively (Figure 9a). The value of S_{EFF} was observed to stabilise very quickly at a value of approximately $\log_{10} S_{EFF} = -2$, which produces a forecast M_{MAX} of 1.7. The largest observed event at PNR-1z had a magnitude of M = 1.5.

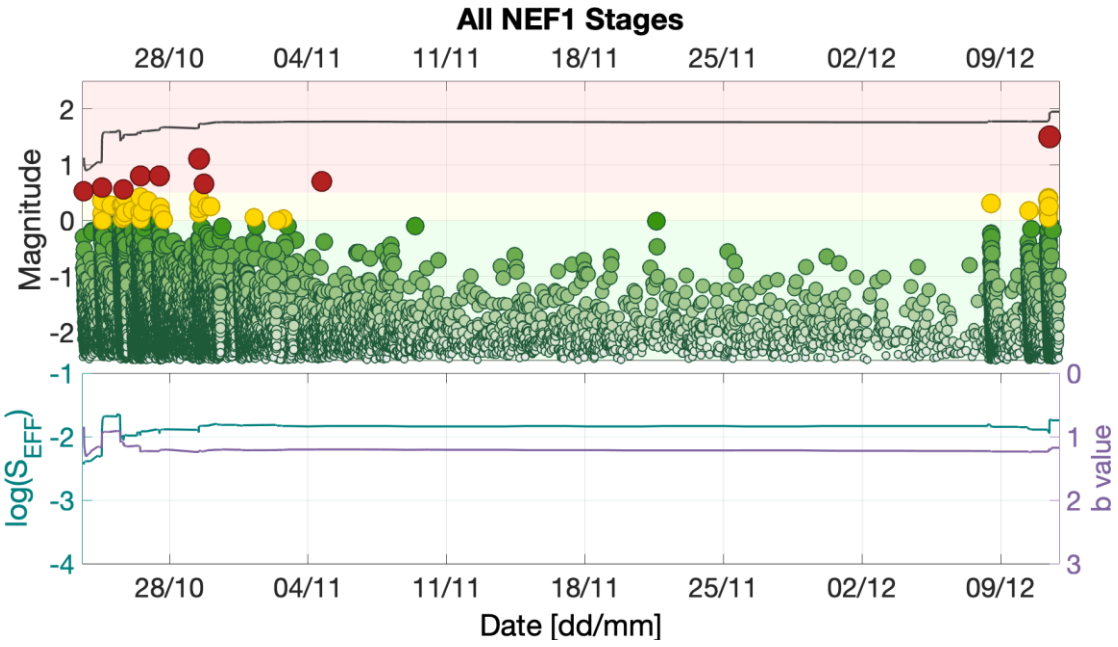

(a)

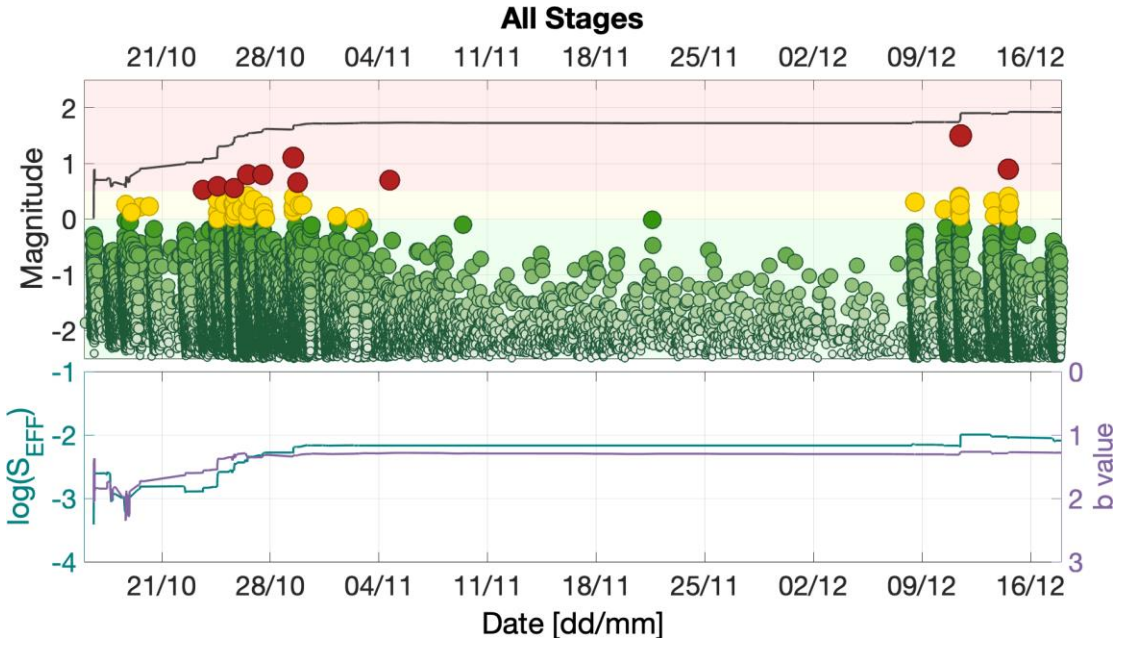

(b)

Figure 9: Forecasting M_{MAX} over cumulative stages. M_{MAX} forecasts when (a) all of the stages that intersect the NEF-1 fault are treated cumulatively, and (b) considering all stages. The observed S_{EFF} is initially at approximately $log_{10} S_{EFF} \approx -3$, giving a forecast $M_{MAX} <$ 1. As the injection begins to interact with the NEF1 feature, the b value decreases and the overall seismic efficiency increases to approximately $log_{10} S_{EFF} \approx -2$, giving a forecast $M_{MAX} < 2$.

For completeness, we also considered the cumulative impacts of the full injection volume and seismicity from all the injection stages (Figure 9b). This represents the worst-case scenario if all of the injected fluid was inducing events on a single seismogenic feature. Initial values for S_{EFF} are low ($\log_{10} S_{EFF} \approx -3$) and *b* values are high ($b > 1.5$) giving $M_{MAX} < 1$. From Stage 18 onwards we observed the hydraulic fracturing interact with the NEF-1 fault, producing an increase in S_{EFF} to ($\log_{10} S_{EFF} \approx -2$) and a decrease in *b* to $b = 1$. This produces an increase in M_{MAX} to $1.5 > M_{MAX} > 2$.

5. Operational Decision-Making

The observations presented above were used by CRL to guide their operational decision-making, especially during the latter injection stages in December, after the period of injection hiatus in November 2018.

During hydraulic fracturing, placement of the proppant cannot begin until fracture breakdown has occurred and fractures begin to propagate. This typically requires a minimum of approximately 80 m^3 of fluid. The proppant concentration is then gradually increased as the injection continues, such that the majority of proppant is placed at the end of the stage. If a stage is terminated mid-way through by a TLS red-light event, only a small proportion of the proppant will have been placed, even if several hundred m^3 of fluid has been injected. In effect, the stage will therefore have been wasted and the environmental water use and seismic risk unnecessarily increased.

At PNR-1z, the modelling described above showed that events larger than $M = 2$ were not expected on the NEF-1 fault given the observed *b* values and seismic efficiency, and the planned injection program. This forecast was reported to the OGA in November 2018, and it falls within the objectives of seismicity mitigation set out by the OGA (minimising felt events and avoiding damaging events). However, the NEF-1 fault could be expected to continue producing $M > 0.5$ red-light events that would terminate injection, preventing the placement of proppant. CRL therefore decided that further injection into the sleeves that intersect the NEF-1 fault would be wasted, and in December 2018 they restarted injection in Stages 37 – 41 at the heel of the well. Based on the seismicity mapping described in Section 3 it was hoped that these stages would pass to the east of the NEF-1 fault, allowing stages to be completed without interruption. Based on the forecasting described in Section 4, CRL was able to do so with confidence if these stages did intersect NEF-1, the levels of seismicity would not exceed the objectives set by the OGA, and therefore injection could be conducted safely.

In reality, some of these latter stages did intersect the NEF-1 fault, triggering two further TLS events with $M > 0.5$. However, the levels of seismicity remained within the levels that had been forecast, as described in the section above.

6. Conclusions

Recent hydraulic fracturing operations at the Preston New Road PNR-1z well were subject to some of the most stringent regulations regarding induced seismicity ever applied to any kind of industrial activity. The operator therefore took a proactive approach to the issue, using real time microseismic monitoring to make operational decisions with respect to induced seismicity. Microseismic observations allowed us to identify the presence of a pre-existing structure on which elevated levels of seismicity was occurring, and to map its extent in the subsurface. This structure produced multiple events that were above the TLS red light

threshold, forcing the operator to stop injection, resulting in wasted stages, where fluid injection ceased before significant quantities of proppant could be placed. Using the microseismic observations, the operator was able to move to injection locations that were less likely to interact with this structure, thereby increasing the chance of conducting successful stages.

At the same time, we used the microseismic observations to populate a statistical model to estimate an upper bound for the largest expected event size during injection. This model was successful in forecasting the magnitudes of the events that did occur. The forecast maximum magnitude of $M = 2$ was within the overall objective set by the regulator to minimise the number of felt events and eliminate the possibility of damaging events. This modelling gave the operator and the regulator confidence that, even if the seismogenic structure were to be intersected by further fracturing stages, the level of risk posed was acceptable. This confidence was borne out during operations: as further activity did occur on the identified fault, but the largest event to occur had a magnitude of $M = 1.5$, matching the forecast expectations.

Various options have been suggested to regulate induced seismicity. Fault respect distances (Westwood *et al*., 2017) require an operator to avoid known faults in the subsurface. However, this case study, along with previous case studies (Igonin *et al*., 2019) shows that reactivated faults may not be visible on 3D seismic surveys, especially if they have strike slip displacement, while imaged faults may not be near to their critical stress and therefore don't reactivate.

Traffic Light Schemes are the most common form of regulation for induced seismicity. The retroactive nature of TLSs means that red light thresholds may be set far lower than the actual level of seismicity that a regulator wishes to prevent. Decisions are based solely on the magnitude of the largest events, which is a reasonable choice if sites are monitored by regional arrays that provide limited detection thresholds and poorly-constrained event locations. However, where operators acquire high-quality real-time microseismic data, providing thousands of accurately-located events across several orders of magnitude, then a TLS that use only the largest event magnitude, and therefore discards 99.9% of the observations available, seems unnecessarily crude. In this paper we have demonstrated how an operator can use microseismicity to assess the seismic risk, and make proactive decisions to mitigate induced seismicity. Such an approach is more in line with the type of goal-setting regulation (Lindøe *et al*., 2012) that has been applied with much success to other aspects of the oil and gas industry. Induced seismicity poses a risk for other forms of sub-surface industrial activity including engineered geothermal systems, and the storage of CO_2 in

geologic reservoirs. As induced seismicity continues to attract public scrutiny, the proactive real-time use of seismic monitoring, as demonstrated here, could see many other applications.

Data and Resources

The event catalogues and injection data used in this paper are scheduled to be released by the Oil and Gas Authority (https://www.ogauthority.co.uk/data-centre/) on the 27th June 2019.

Acknowledgements

We would like to thank Cuadrilla Resources and their joint venture partners Spirit Energy and A J Lucas for collaboration on this project. We would like to thank the BGS for providing data from the additional surface stations that were installed at the site. We would also like to thank Schlumberger for processing the monitoring data in real time. JPV was funded by NERC Grant NE/R018162/1, TK was supported by the NERC GW4+ Doctoral Training Partnership (Grant NE/L002434/1), and JMK and AFB were funded by NERC Grant NE/R018006/1.

References

Aki K., 1965. Maximum likelihood estimate of b in the formula $\log N = a - bM$ and its confidence limits: Bulletin of the Earthquake Research Institute, University of Tokyo 43, 237-239.

Akkar S., M.A. Sandikkaya, J.J. Bommer, 2014. Empirical ground-motion models for point- and extended-source crustal earthquake scenarios in Europe and the Middle East: Bulletin of Earthquake Engineering 12, 359-387.

Atkinson, G.M., D.W. Eaton, H. Ghofrani, D. Walker, B. Cheadle, R. Schultz, R. Shcherbakov, K. Tiampo, J. Gu, R.M. Harrington, Y. Liu, M. van der Baan, H. Kao, 2016. Hydraulic fracturing and seismicity in the Western Canada Sedimentary Basin: Seismological Research Letters 87, 631-647.

Baisch S., C. Koch, A. Muntendam-Bos, 2019. Traffic Light Systems: To what extent can induced seismicity be controlled: Seismological Research Letters, in press.

Bao X. and D.W. Eaton, 2016. Fault activation by hydraulic fracturing in western Canada: Science 354, 1406-1409.

Butcher A., R. Luckett, J.P. Verdon, J-M. Kendall, B. Baptie, J. Wookey, 2017. Local magnitude discrepancies for near-event receivers; implications for the UK traffic light scheme: Bulletin of the Seismological Society of America 107, 532-541.

Cuadrilla Resources Ltd., 2018. Preston New Road 1z Hydraulic Fracture Plan. Accessed at: https://consult.environment-agency.gov.uk/onshore-oil-and-gas/information-on-cuadrillas-preston-new-road-site/supporting_documents/Preston%20New%20Road%20HFP.pdf on 25/3/2019.

534 Chambers K., J-M. Kendall, S. Brandsberg-Dahl, J. Rueda, 2010. Testing the ability of surface
535 arrays to monitor microseismic activity: Geophysical Prospecting 58, 821-830.
536 Clarke H., L. Eisner, P. Styles, P. Turner, 2014. Felt seismicity associated with shale gas
537 hydraulic fracturing: The first documented example in Europe: Geophysical Research
538 Letters 41, 8308-8314.
539 Clauset A., C.R. Shalizi, M.E.J. Newman, 2009. Power-law distributions in empirical data:
540 Society for Industrial and Applied Mathematics Review 51, 661-703.
541 Friberg P.A., G.M. Besana-Ostman, I. Dricker, 2014. Characterisation of an earthquake
542 sequence triggered by hydraulic fracturing in Harrison County, Ohio: Seismological
543 Research Letters 85, 1295-1307.
544 Green C.A., P. Styles, B.J. Baptie, 2012. Preese Hall shale gas fracturing review and
545 recommendations for induced seismic mitigation. Department of Energy and Climate
546 Change, London.
547 Grigoli F., S. Cesca, A.P. Rinaldi, A. Manconi, J.A. López-Comino, J.F. Clinton, R.
548 Westaway, C. Cauzzi, T. Dahm, S. Wiemer, 2018. The November 2017 MW 5.5. Pohang
549 earthquake: A possible case of induced seismicity in South Korea: Science 360, 1003-
550 1006.
551 Gutenberg B., and C.F. Richter, 1944. Frequency of earthquakes in California: Bulletin of the
552 Seismological Society of America 34, 185-188.
553 Hallo M., I. Oprsal, L. Eisner, M.Y. Ali, 2014. Prediction of magnitude of the largest
554 potentially induced seismic event: Journal of Seismology 18, 421-431.
555 Hammack R., W. Harbert, S. Sharma, B. Stewart, R. Capo, A. Wall, A. Wells, R. Diehl, D.
556 Blaushild, J. Sams, G. Veloski, 2014. An Evaluation of Fracture Growth and Gas/Fluid
557 Migration as Horizontal Marcellus Shale Gas Wells are Hydraulically Fractured in Greene
558 County, Pennsylvania: EPAct Technical Report Series, U.S. Department of Energy,
559 National Energy Technology Laboratory, Pittsburgh, PA, NETL-TRS-3-2014.
560 Hansard, 2018. House of Commons Official Report 649(208), 714-716.
561 Häring M.O., U. Schanz, F. Ladner, B.C. Dyer, 2008. Characterisation of the Basel 1 enhanced
562 geothermal system: Geothermics 37, 469-495.
563 Igonin N., J.P. Verdon, J-M. Kendall, D.W. Eaton, 2019. The importance of pre-existing
564 fracture networks for fault reactivation during hydraulic fracturing: Proceedings of the
565 National Academy of Sciences, *sub judice*.
566 Kendall J-M., A. Butcher, A.L. Stork, J.P. Verdon, R. Luckett, B.J. Baptie, 2019. How big is a
567 small earthquake? Challenges in determining microseismic magnitudes: First Break 37, 51-
568 56.
569 Keranen K.M., M. Weingarten, G.A. Abers, B.A. Bekins, S. Ge, 2014. Sharp increase in central
570 Oklahoma seismicity since 2008 induced by massive wastewater injection: Science 345,
571 448-451.
572 Kettlety T., J.P. Verdon, M.J. Werner, J-M. Kendall, J. Budge, 2019. Investigating the role of
573 elastostatic stress transfer during hydraulic fracturing-induced fault reactivation:
574 Geophysical Journal International 217, 1200-1216.
575 Lindøe P.H., M. Baram, J. Paterson, 2012. Robust Offshore Risk Regulation – an assessment
576 of US, UK and Norwegian approaches: European Safety and Reliability Conference,
577 Helsinki.
578 Luckett R., L. Ottemoller, A. Butcher, B. Baptie, 2019. Extending local magnitude M_L to
579 short distances: Geophysical Journal International 216, 1145-1156.
580 Maxwell S.C., J. Shemeta, E. Campbell, D. Quirk, 2008. Microseismic deformation rate
581 monitoring: SPE Annual Technical Conference, SPE116596.

582 Maxwell S.C., M. Jones, R. Parker, S. Miong, S. Leaney, D. Dorval, D. D'Amico, J. Logel, E.
583 Anderson, K. Hammermaster, 2009. Fault activation during hydraulic fracturing: SEG
584 Annual Meeting Expanded Abstracts 28, 1552-1556.
585 Maxwell S.C., J. Rutledge, R. Jones, M. Fehler, 2010. Petroleum reservoir characterization
586 using downhole microseismic monitoring: Geophysics 75, A129-A137.
587 Oil and Gas Authority, 2018. Consolidated Onshore Guidance, Version 2.2. Oil and Gas
588 Authority, London. Accessed at:
589 https://www.ogauthority.co.uk/media/4959/29112017_consolidated-onshore-guidance-
590 compendium_vfinal-002.pdf on 5/04/2019.
591 Schultz R., V. Stern, M. Novakovic, G. Atkinson, Y.J. Gu, 2015a. Hydraulic fracturing and the
592 Crooked Lake sequences: Insights gleaned from regional seismic networks: Geophysical
593 Research Letters 42, 2750-2758.
594 Shapiro S.A., C. Dinske, C. Langenbruch, 2010. Seismogenic index and magnitude
595 probability of earthquakes induced during reservoir fluid stimulations: The Leading Edge
596 29, 304-309.
597 Skoumal R.J., M.R. Brudzinski, B. S. Currie, 2015. Induced earthquakes during hydraulic
598 fracturing in Poland Township, Ohio: Bulletin of the Seismological Society of America
599 105, 189-197.
600 van der Elst, N.J., M.T. Page, D.A. Weiser, T.H.W. Goebel, S.M. Hosseini, 2016. Induced
601 earthquake magnitudes are as large as (statistically) expected: Journal of Geophysical
602 Research 121, 4575-4590.
603 Verdon J.P., 2014. Significance for secure CO_2 storage of earthquakes induced by fluid
604 injection: Environmental Research Letters 9, 064022.
605 Verdon J.P. and J. Budge, 2018. Examining the capability of statistical models to mitigate
606 induced seismicity during hydraulic fracturing of shale gas reservoirs: Bulletin of the
607 Seismological Society of America 108, 690-701
608 Wang Z. and A. Krupnick, 2013. A retrospective review of shale gas development in the
609 United States: What lead to the boom?: Resources for the Future DP 13-12.
610 Webster B., 2018. Cuadrilla to resume fracking seven years after tremors: The Times, 16th
611 October 2018. Accessed at: https://www.thetimes.co.uk/article/cuadrilla-to-resume-
612 fracking-seven-years-after-tremors-h6lrndhxj on 28/3/2019.
613 Wessels, S.A., A. De La Peña, M. Kratz, S. Williams-Stroud, T. Jbeili, 2011. Identifying
614 faults and fractures in unconventional reservoirs through microseismic monitoring: First
615 Break 29, 99-104.
616 Westwood R.F., S.M. Toon, P. Styles, N.J. Cassidy, 2017. Horizontal respect distance for
617 hydraulic fracturing in the vicinity of existing faults in deep geological reservoirs: a
618 review and modelling study: Geomechanics and Geophysics for Geo-Energy and Geo-
619 Resources 3, 379-391.
620 Zinno R., J. Gibson, R.N. Walker Jr, R.J. Withers, 1998. Overview: Cotton Valley hydraulic
621 fracture imaging project: SEG Annual Meeting Expanded Abstracts 17, 338-341.
622
623
624
625
626